

THE GALACTIC INNER HALO: SEARCHING FOR WHITE DWARFS AND MEASURING THE FUNDAMENTAL GALACTIC CONSTANT, Θ_{\circ}/R_{\circ} ¹

Jasonjot Singh Kalirai², Harvey B. Richer², Brad M. Hansen³, Peter B. Stetson⁴, Michael M. Shara⁵, Ivo Saviane⁶, R. Michael Rich³, Marco Limongi⁷, Rodrigo Ibata⁸, Brad K. Gibson⁹, Gregory G. Fahlman⁴ & James Brewer²

ABSTRACT

We establish an extragalactic, zero-motion frame of reference within the deepest optical image of a globular star cluster, a *Hubble Space Telescope* (*HST*) 123-orbit exposure of M4 (GO 8679, cycle 9). The line of sight beyond M4 ($l, b = 351^{\circ}, 16^{\circ}$) intersects the inner halo (spheroid) of our Galaxy at a tangent-point distance of 7.6 kpc (for $R_{\circ} = 8$ kpc). The main sequence of this population can be clearly seen on the color-magnitude diagram (CMD) below the M4 main sequence.

¹Based on observations with the NASA/ESA Hubble Space Telescope, obtained at the Space Telescope Science Institute, which is operated by AURA under NASA contract NAS 5-26555. These observations are associated with proposal GO-8679.

²Department of Physics & Astronomy, University of British Columbia, 6224 Agricultural Road, Vancouver, BC V6T 1Z1, Canada. jkalirai@astro.ubc.ca, richer@astro.ubc.ca, jbrewer@astro.ubc.ca

³Department of Physics & Astronomy, University of California at Los Angeles, Math-Sciences 8979, Los Angeles, CA 90095-1562. hansen@astro.ucla.edu, rmr@astro.ucla.edu

⁴National Research Council of Canada, Herzberg Institute of Astrophysics, 5071 West Saanich Road, RR5, Victoria, BC V9E 2E7, Canada. peter.stetson@nrc.gc.ca, Greg.Fahlman@nrc.gc.ca

⁵American Museum of Natural History, Astrophysics Department, Central Park West & 79th Street, New York, NY 10024-5192. mshara@amnh.org

⁶European Southern Observatory, Alonso de Cordova 3107, Vitacura, Casilla 19001, Santiago 19, Chile. isaviane@eso.org

⁷Osservatorio Astronomico di Roma, Via Frascati 33, I-00040 Monte Porzio Catone, Rome, Italy. marco@nemo.mporzio.astro.it

⁸Observatoire de Strasbourg, 11 rue de l'Universite, F-67000 Strasbourg, France. ibata@newb6.u-strasbg.fr

⁹Centre for Astrophysics and Supercomputing, Swinburne University, Mail 31, P.O. Box 218, Hawthorn, Victoria, 3122 Australia. bgibson@astro.swin.edu.au

We isolate these spheroid stars from the cluster on the basis of their proper motions over the 6-year baseline between these observations and others made at a previous epoch with *HST* (GO 5461, cycle 4). Distant background galaxies are also found on the same sight line by using image-morphology techniques. This fixed reference frame allows us to determine an independent measurement of the fundamental Galactic constant, $\Omega_{\circ} = \Theta_{\circ}/R_{\circ} = 25.3 \pm 2.6$ km/s/kpc, thus providing a velocity of the Local Standard of Rest $v_{\text{LSR}} = \Theta_{\circ} = 202.7 \pm 24.7$ km/s for $R_{\circ} = 8.0 \pm 0.5$ kpc. Secondly, the galaxies allow a direct measurement of M4’s absolute proper motion, $\mu_{\alpha}\hat{\alpha} = -12.26 \pm 0.54$ mas/yr, $\mu_{\delta}\hat{\delta} = -18.95 \pm 0.54$ mas/yr, in excellent agreement with recent studies. The clear separation of galaxies from stars in these deep data also allow us to search for inner-halo white dwarfs. We model the conventional Galactic contributions of white dwarfs along our line of sight and predict 7.9 (thin disk), 6.3 (thick disk) and 2.2 (spheroid) objects to the limiting magnitude at which we can clearly delineate stars from galaxies ($V \sim 29$). An additional 2.5 objects are expected from a 20% white dwarf dark halo consisting of $0.5 M_{\odot}$ objects, 70% of which are of the DA type. After considering the kinematics and morphology of the objects in our data set, we find the number of white dwarfs to be consistent with the predictions for each of the conventional populations. However, we do not find any evidence for dark halo white dwarfs.

Subject headings: Dark matter – Galaxy: halo, kinematics and dynamics – galaxies: photometry – globular clusters: individual (Messier 4) – stars: white dwarfs

1. Introduction

A recent *HST* imaging project of the Galactic globular cluster M4 (GO 8679) has so far investigated both the low-mass end of the hydrogen burning main sequence (Richer et al. 2002) and the termination of the white dwarf cooling sequence (Hansen et al. 2002). The data for the cluster members was isolated from background/foreground contaminants by using the proper motion of the cluster with respect to the field over a 6 year baseline (previous epoch data obtained with *HST* in cycle 4, 1995 (Richer et al. 1995; Richer et al. 1997; Ibata et al. 1999)). Richer et al. (2002) found the M4 cluster mass function to be slowly rising to low masses. In Hansen et al. (2002), the cluster white dwarfs were used as chronometers to provide an age estimate of 12.70 ± 0.35 Gyrs ($1\text{-}\sigma$) largely independent of the turn-off for M4. In this contribution, we shift our focus to the background contamination itself (the spheroid and galaxies) and isolate these populations for investigation. A separate contribu-

tion will address the main-sequence stars, luminosity and mass functions of the spheroid, and foreground thin/thick disk components.

Stars, gas and dust in the disk, bulge and spheroid of our Galaxy only account for $\sim 10\%$ of the total mass within $R = 50$ kpc (Wilkinson & Evans 1999). The remaining mass is believed to reside in the dark halo of our Galaxy (dark matter), and determining the nature of this mass is a critical issue today in astrophysics. Recently, the MACHO project has analyzed data from microlensing events in the direction of the LMC and determined that the mean mass of the lenses is $0.5 \pm 0.3 M_{\odot}$, with a $\sim 20\%$ MACHO fraction (Alcock et al. 2000). This naturally suggests faint white dwarfs as the source of these lenses. Even if the MACHOs cannot account for the total dark matter contribution, determining the properties and number density of faint halo white dwarfs is important in several areas of astrophysics. These include studying the IMF of population III stars (through their remnants) and constraining the star-formation history of our Galaxy.

Studying white dwarfs in the Galactic bulge or spheroid from the ground is difficult for two reasons. First, the end of the white dwarf cooling sequence for $0.5 M_{\odot}$ objects in a population 12 Gyrs old is $M_V \sim 17$ (Hansen 1999), which, at the center of the Galaxy (8 kpc), is $V > 31.5$. The depth of the M4 study ($V \sim 30$), however, is faint enough to detect the brighter end of this cooling sequence. Secondly, piercing through the disk of our Galaxy picks up many foreground metal-rich disk stars which contaminate the sample. Although observing at higher latitudes above the center helps avoid the thick disk, the resulting spheroid number density also drops off rapidly, $n(r) \propto r^{-3.5}$ (Binney & Merrifield 1998). With HST we can achieve the depth required to measure these faint stars, but there are several disadvantages. First, we are dealing with small-number statistics due to the limited field of view (for instance, WFPC2 has a field area of 5.7 arcmin²). More importantly, long exposures pick up many galaxies, such as seen in the HDF, which can mimic stars in faint photometry.

Given the caveats listed above, we attempt in this paper to isolate potential white dwarfs in the field by separating out populations using both their morphology and their kinematics. After briefly presenting the data in §2, we begin by finding galaxies and establishing our extragalactic zero-motion frame of reference. This then allows us to determine two important quantities directly measured from a sample of extragalactic objects: the velocity of the Local Standard of Rest (§3.3) and the absolute proper motion of M4 (§3.4). In §4 we examine the different populations which make up the corrected proper-motion and color-magnitude diagrams and discuss the spheroid population. Next, we analyze faint, blue stars in this population and identify our best candidates for disk and spheroid white dwarfs (§5). This includes comparing our results to the expected numbers of white dwarfs given the searchable volume in our data and the various population-density distributions along the line of sight.

In §6, we discuss the current status of the search for dark halo white dwarfs as well as some of the different views which have been presented in the recent literature. The current results are placed in the context of these independent efforts. The overall study is concluded in §7.

2. The Data

The data (35 hours in F606W, 55 hours in F814W) for the present and previous observations (1995 - cycle 4 (Richer et al. 1995; Richer et al. 1997; Ibata et al. 1999)) were reduced using the DAOPHOT/ALLSTAR (Stetson 1987) and ALLFRAME (Stetson 1994) photometry packages. Individual frames were registered and co-added using the DAOMASTER and MONTAGE2 programs. For this we transformed all images for a given CCD to a common coordinate system for each epoch and filter and combined the images using standard IRAF tasks. As the fields are dominated by M4 cluster members, smaller matching radii rejected non cluster members. A plot showing dx vs dy between the older and newer epochs therefore shows the cluster stars grouped at the origin and a secondary group of stars offset from this. The transformations were then iterated using a list of stars likely to be cluster members as selected from this clump near the origin. The CMD of the resulting stars verified their cluster origin. The list of these stars were then transformed back onto each of the individual frames which were reduced using ALLSTAR, with the recentering option enabled. The output ALLSTAR files, which contain only cluster members, were matched with DAOMASTER using a 20-term transformation equation. The 20-term transformation was found to reduce systematic errors significantly from the 6-term transformation. We produced histograms of dx and dy for the cluster stars and minimized streaming motions near the edges of the CCD caused by distortions by reducing the matching radius until it was similar in magnitude to the rms error in the transformation. The residual systematic bias in the proper motion diagram is evaluated below. Finally, MONTAGE2 was used to expand the frames by a factor of 3 before registering them as noted above. This procedure is similar to a drizzling routine and effectively decreased the cluster proper-motion dispersion in the proper-motion diagram.

The final photometry list includes only those stars which were measured in both filters and at both epochs, and which passed a visual inspection. Further details of the reduction and calibration of the data set used in this analysis will be described in Richer et al. (2003) (see also §2 of Richer et al. (2002)). We summarize the key parameters for both the cluster and field population and present the observational log in Table 1.

In Figure 1, we present the proper-motion diagram for our data. The motion of the cluster with respect to the field (6 year baseline), can be clearly seen as the tight clump

toward negative proper motions. For the units, we first translated the x and y pixel motions into Galactic coordinates (l, b) by using a rotation angle which aligned the y axis of the CCD to the North Galactic Pole. To express these proper motions, we adopt the convention that the vector proper motion is given by $\mu = \sqrt{(\mu_l \hat{\mathbf{l}})^2 + (\mu_b \hat{\mathbf{b}})^2}$, where $\hat{\mathbf{l}}$ and $\hat{\mathbf{b}}$ are unit vectors in the corresponding directions. We then converted the HST WFPC2 pixels into arcseconds using the plate scale ($0''.1/\text{pixel}$, Biretta et al. 2002) of the CCD. The motions are then divided by the baseline of 6 years and converted to mas/yr. Zero motion in the diagram, $(\mu_l \hat{\mathbf{l}}, \mu_b \hat{\mathbf{b}}) = (0, 0)$, is centered on well measured, bright galaxies (larger red dots) and is described in detail in §3.2. A small systematic bias, seen as a stretching of the proper-motion diagram in the l direction, is evaluated to be 0.26 mas/yr. This was measured by producing histograms of the proper-motion diagram for different magnitude cuts. Comparing the dispersions in the l and b directions for the brightest stars directly gives the error. This systematic bias has been factored into the error budget for all measurements.

3. An Extragalactic Reference Frame

3.1. Measuring Galaxies

Isolating galaxies in the current study is crucial as they can mimic faint blue white dwarfs in the data. Additionally, since the galaxies are not moving, they represent a fixed zero-motion position in the proper-motion diagram from which we can measure absolute motions. Visually, the images of M4 only show a small number of obvious galaxies. Were it not for the greatly larger number of foreground stellar objects, the 1.3 magnitudes of foreground visual extinction and the higher background produced by scattered light and zodiacal light, this image would likely look similar to the HDF (Williams et al. 1996) which shows 1781 galaxies in the range $26 \leq V_{\text{AB}} \leq 29.5$.

To measure galaxies in our field, we used the image morphology classification tool, SExtractor (Bertin & Arnouts 1996). SExtractor assigns a stellarity index to each object which can be used to distinguish between stars and galaxies. The stellarity is determined through a neural network, which learns based on other, high signal-to-noise, stars. Although SExtractor was not able to recover statistics for every object that ALLSTAR measured in our data, the classifications are $\sim 75\%$ complete through $V = 24\text{--}29$. Fainter than $V = 29$, SExtractor was only able to measure $\sim 40\%$ of the ALLSTAR sources and struggled to classify objects as stars or galaxies. Altogether, just over 50 galaxies were identified and measured using a stellarity < 0.2 cut.

Figure 2 (top) shows the SExtractor classifications as a function of magnitude for all

objects. The distribution of points on this diagram can be broken into two classes which are separated by the horizontal lines. The stars are found predominantly in a clump near $\text{stellarity} = 1$ down to a magnitude of $V \sim 28$. Fainter than this, the classifications are not as good. However a clump of stars can be seen extending to $V \sim 29$ with a sharp cutoff in stellarity at 0.7. The galaxies are found near the bottom of the figure, at $\text{stellarity} = 0$. Here we have chosen a conservative $\text{stellarity} < 0.2$ cut to include possible outliers above the predominant galaxy sequence. Very few objects ($\sim 4\%$ for $V < 29$) are seen between the stars and galaxies indicating that the classifications are reliable. At the faintest magnitudes, $V \sim 29$, a clump of objects can be seen at $\text{stellarity} = 0.5$. This is expected as the program will, on average, choose $\text{stellarity} = 0.5$ for an object which it cannot classify. Shape parameter comparisons from artificial star tests also confirm that the stellarity is measured accurately down to this limit. Therefore $V \sim 29$ represents the limit at which we can accurately separate stars from galaxies.

In Figure 2 (bottom) we use the stellarity to illustrate the separate populations in our data. Here, the stellarity of all objects is plotted against the total absolute proper motion, $\mu_{\text{total}} = \sqrt{(\mu_l \hat{\mathbf{l}})^2 + (\mu_b \hat{\mathbf{b}})^2}$ as determined with respect to the center of the large red dots in Figure 1. We will justify this location in the next section. First, we note two clear clumps for stars (at constant $\text{stellarity} \sim 1$) representing the cluster ($\mu_{\text{total}} \sim 22.5$ mas/yr, with a small dispersion) and field populations ($\mu_{\text{total}} \sim 5$ mas/yr, with a much larger dispersion). This bi-modality continues for lower stellarities down to $\text{stellarity} \sim 0.7$. The galaxies ($\text{stellarity} \sim 0$) are obviously found at low μ_{total} . However, a tail is seen to higher proper-motion displacements (these are the small red dots in Figure 1). As we will see in §3.2, this tail represents the faintest galaxies and indicates that our ability to measure the proper motions has degraded due to reduced signal-to-noise.

3.2. Centering the Zero-Motion Frame of Reference

In Figure 1, we showed the locations of bright, well-measured galaxies (large red dots) which represent an absolute background reference frame. As these galaxies clumped together, we first estimated their position and measure the absolute proper motion of all objects with respect to this point.

Figure 3 shows the total proper-motion displacement as a function of magnitude for both stars (top) and galaxies (bottom). The distributions are found to be very different. The stars behave as expected and are confined within a constant envelope in μ_{total} across all but the faintest magnitudes. Note that the spread in the distribution of M4 cluster members ($\mu_{\text{total}} \sim 22.5$ mas/yr) for $V \geq 28$ is not due to the main-sequence stars. At $V \gtrsim 28$, the main

sequence of M4 contains very few stars (Richer et al. 2002) and so the scatter is due to the faintest white dwarfs in the cluster. On the other hand, the total proper-motion displacement of the galaxies (bottom) is found to completely degrade for $V \gtrsim 27$. Considering that we know from Figure 2 that the stellarities for the galaxies are measured accurately to well beyond this limit, this flaring must be entirely due to difficulties in the astrometric centering on these faint extended sources. Therefore the galaxies with $V \lesssim 27$ should dictate the location of the zero-motion frame as some of their fainter counterparts have been poorly measured. The centroid of the 12 galaxies which satisfy this criteria represents the zero-motion frame of reference shown on all proper-motion diagrams (see large red dots in Figure 1). The one-dimensional error in this location is calculated as $\sigma/\sqrt{N} \approx 0.5$ mas/yr, where σ is the proper-motion dispersion of the galaxy sample (~ 1.6 mas/yr).

3.3. The Circular-Speed Curve

We now use the extragalactic stationary frame of reference established above to measure two important quantities. The first, the circular-speed curve, is a plot of the velocity of a test particle (Θ_\circ) moving in a circular orbit in the Galactic plane and around the Galactic center, vs the distance R at which it is located relative to the center. The ratio of these quantities at the Solar radius ($\Omega_\circ = \Theta_\circ/R_\circ$) represents one of the more difficult problems in Galactic structure and directly provides the mass interior to R_\circ . This constant is fundamentally important in understanding the dynamics of the Galactic halo and the Local Group.

For the motion in the Galactic plane, we measure an angular proper motion from the center of the galaxy clump to the center of the spheroid clump of $\mu_l \hat{\mathbf{l}} = -5.53 \pm 0.56$ mas/yr. The spheroid clump was chosen by first eliminating foreground disk stars by overplotting a solar metallicity disk dwarf fiducial on our CMD (presented in §4). These disk stars represent the redder, brighter stars located above M4. We then removed both M4 and galaxies, and iteratively determined the center of the inner halo based on σ -clipping to remove outliers. The resulting population is shown within the large circle in Figure 1. Assuming the spheroid is not rotating (see below), the vector motion of $\mu_l \hat{\mathbf{l}} = -5.53 \pm 0.56$ mas/yr represents the reflex motion of the Sun, a combination of the LSR circular orbit and the deviation of the Sun from that circular orbit (Solar motion). The uncertainty in this number is derived from the quadrature sum of the dispersions in each of the galaxy and spheroid clumps. We can correct this observed proper motion for the known Solar motion in the Galactic plane, $v_\odot = 5.25 \pm 0.62$ km/s in the direction of Galactic rotation (Dehnen & Binney 1998). Orienting this Solar motion onto the l direction, we find a correction of $\Delta\mu_l \hat{\mathbf{l}} = 0.19 \pm 0.02$ mas/yr. Therefore, $\Omega_\circ = \Theta_\circ/R_\circ = -4.74\mu_l \hat{\mathbf{l}} = 25.3 \pm 2.6$ km/s/kpc.

The angular velocity of the circular rotation of the Sun can be directly compared to the Oort Constants, A and B (Kerr & Lynden-Bell 1986), which measure the shear and vorticity of the disk. Recent analysis based on *Hipparcos* measurements of 220 Galactic Cepheids gives $\Omega_{\odot} = A - B = 27.19 \pm 0.87$ km/s/kpc (Feast & Whitelock 1997), larger than our value but consistent within the uncertainty. Other measurements, such as the Sgr A* proper-motion study (Reid et al. 1999), also find a higher value than ours, $\Omega_{\odot} = 27.2 \pm 1.7$ km/s/kpc. At $R_{\odot} = 8.0 \pm 0.5$ kpc, these two measurements give a Solar reflex velocity of $v_{\text{LSR}} = \Theta_{\odot} \sim 218$ km/s, in good agreement with the independent IAU adopted value of 220 ± 15 km/s (Binney & Tremaine 1987) based on kinematics of high velocity stars. The most recent study by Bedin et al. (2003) uses a single QSO in a different field of M4 than studied here and finds $\Omega_{\odot} = 27.6 \pm 1.7$ km/s/kpc. However, other studies, such as Kuijken & Tremaine (1994) find much smaller values. Based on a set of self-consistent solutions for different Galactic parameters, they find $v_{\text{LSR}} = 180$ km/s. Merrifield (1992) also calculates a lower Local Standard of Rest velocity, $v_{\text{LSR}} = 200 \pm 10$ km/s, using rotation of H I layers. For $R_{\odot} = 8.0 \pm 0.5$ kpc, our result gives a similar value to this latter study, $v_{\text{LSR}} = 202.7 \pm 24.7$ km/s. Only 15% of the uncertainty in our result is contributed by the 0.5 kpc uncertainty in the Galactocentric distance with the remaining error almost entirely due to the dispersion in the galaxy sample. The dispersion in the spheroid sample is calculated from those stars within the circle in Figure 1 and has also been folded into this uncertainty.

Although our value for Ω_{\odot} is lower than some previous studies of the circular speed curve, it is consistent with those studies within the $1\text{-}\sigma$ uncertainty. One consideration that we are currently investigating is possible rotation by the spheroid itself, which would cause an over/underestimate of the Solar reflex motion depending on the degree to which stars in front of the tangent point dominate over stars behind it. Given the small field of view, we could also potentially be affected by debris tails or small groups of stars with peculiar orbits. Despite these caveats, we stress the importance of this measurement. Kuijken & Tremaine (1994) estimate that if they are correct and a reduction of Θ_{\odot} from 220 km/s to 180 km/s is needed, the line-of-sight velocity of M31 relative to the Galactic center would correspondingly increase by 25%. This, in turn, would increase the mass of the Local Group from timing arguments by 35%. Although additional methods (see Kuijken & Tremaine 1994 for a summary) to constrain the circular-speed curve are being used (e.g., using Local Group kinematics, motions of globular clusters or halo stars, tangent-point measurements of the inner rotation curve and outer-rotation curve-measurements using OB stars and H II regions, etc.), they are not superior to measurements made with extragalactic reference frames. These global measurements, such as the present work and the Sgr A* proper motions (Backer & Stramek 1999; Reid et al. 1999), avoid Galactic variations in the sample of objects and therefore reduce systematic uncertainties (Binney & Tremaine 1987).

The apparent motion of the spheroid stars in the direction perpendicular to the plane is very small, $\mu_b \hat{\mathbf{b}} = -0.32 \pm 0.56$ mas/yr (see Figure 1). The correction for the component of the known Solar motion, $v_{Z_\odot} = 7.17 \pm 0.38$ km/s (Dehnen & Binney 1998) in this direction is $\Delta\mu_b \hat{\mathbf{b}} = -0.12 \pm 0.01$ mas/yr. Therefore, the residual velocity for $R_o = 8.0 \pm 0.5$ kpc is found to be 7.4 ± 21.2 km/s, consistent with a stationary population.

3.4. The Absolute Proper Motion of M4

The space motions of Galactic globular clusters are of interest in order to constrain and reconstruct their orbits around the Galaxy. This yields important information on cluster origins and destruction processes, as well as Galactic dynamics. Formation scenarios of the Galaxy can be better understood by coupling the kinematics of the clusters with other properties, such as the metallicities and ages (Dinescu et al. 1997).

Three primary methods exist to determine the space motions of globular clusters and all involve measuring the absolute proper motion of the stars in the cluster. The indirect methods involve either using secular parallaxes (which require a knowledge of Galactic rotation) or using the new ‘bulge-relative’ method (which requires the distance and proper motion of the bulge: Terndrup et al. 1998). The preferred method involves using extragalactic objects, galaxies or QSOs, and directly measuring the motion of the cluster.

Only three previous estimates of the M4 absolute proper motion exist in the literature. Cudworth & Rees (1990) used bright field stars as a reference to the brighter cluster stars to estimate $\mu_\alpha \hat{\boldsymbol{\alpha}} = -11.6 \pm 0.7$ mas/yr, $\mu_\delta \hat{\boldsymbol{\delta}} = -16.3 \pm 0.9$ mas/yr. Dinescu et al. (1999) used *Hipparcos* field stars as a reference to carefully measure the motion of the cluster after accounting for plate-transformation systematics: $\mu_\alpha \hat{\boldsymbol{\alpha}} = -12.50 \pm 0.36$ mas/yr, $\mu_\delta \hat{\boldsymbol{\delta}} = -19.93 \pm 0.49$ mas/yr. The Bedin et al. (2003) study finds $\mu_\alpha \hat{\boldsymbol{\alpha}} = -13.21 \pm 0.35$ mas/yr, $\mu_\delta \hat{\boldsymbol{\delta}} = -19.28 \pm 0.35$ mas/yr. Here we present an absolute proper-motion measurement of the cluster measured with respect to a sample of galaxies, an important measurement considering that M4 is a very well studied cluster.

As discussed earlier, our coordinate differences were measured by centering on the cluster stars. We then found the center of the extragalactic distribution and directly measured the difference between this and the center of the M4 clump. Converting Galactic coordinates to the equatorial system, we find $\mu_\alpha \hat{\boldsymbol{\alpha}} = -12.26$ mas/yr, $\mu_\delta \hat{\boldsymbol{\delta}} = -18.95$ mas/yr, with a one-dimensional uncertainty of 0.54 mas/yr. The error in the mean for the absolute proper motion is the quadrature sum of the total errors for each of the galaxy and cluster star distributions. We’ve also factored in the 0.26 mas/yr systematic bias discussed in §2. The

final errors in our absolute proper motion are completely dominated by the dispersion in the galaxy sample. Comparing these results directly to previous studies, we find that our total proper motion ($\mu_{\text{total}} = \sqrt{(\mu_{\alpha}\hat{\alpha})^2 + (\mu_{\delta}\hat{\delta})^2}$) is $\sim 4\%$ smaller than the Dinescu et al. (1999) value, $\sim 13\%$ larger than the Cudworth & Rees (1990) value and $\sim 3\%$ smaller than the Bedin et al. (2003) study.

For completeness, we can also convert our cluster proper motions into absolute space motions. The Solar motion is $(U_{\odot}, V_{\odot}, W_{\odot}) = (+10.0, +5.2, +7.2)$ km/s (Dehnen & Binney 1998), where U_{\odot} is positive towards the Galactic center, V_{\odot} is in the direction of Galactic rotation, and W_{\odot} is out of the plane. Therefore, for M4 we derive an absolute space motion of $(U, V, W)_{\circ} = (57.0 \pm 6.3, -186.1 \pm 6.3, -2.4 \pm 4.5)$ km/s with respect to the LSR, for a distance of $d_{\text{M4}} = 1720$ pc and a cluster radial velocity of $v_r = 70.9 \pm 0.6$ km/s (Peterson, Rees & Cudworth 1995). The uncertainties calculated for the space motions above do not include any distance uncertainty.

4. The Proper-Motion and Color-Magnitude Diagrams

In Figure 4 we again present the final proper-motion diagram and also the corresponding color-magnitude diagram for all objects within the M4 field. As we mentioned earlier, the tighter clump of dots in the proper-motion diagrams represent M4 (proper-motion dispersion, $\sigma_{\text{total}} = 1.9$ mas/yr) whereas the more diffuse clump represents the spheroid population plus other stars along the line of sight (proper-motion dispersion $\sigma_{\text{total}} = 3.7$ mas/yr). The dispersions in these cases actually measure a combination of each population’s intrinsic velocity dispersion as well as scatter produced from instrumental errors. The latter is clearly evident as we get smaller dispersions for brighter magnitude cuts which eliminate the lowest signal-to-noise ratio objects (the above numbers however do reflect the dispersions measured from using the entire data set). A detailed analysis of the intrinsic dispersion, after correcting for instrumental scatter, will be provided in Saviane et al. (2003). The extragalactic objects in our data, which have not moved during the 6 year baseline, are also convolved within the field clump identified above. These are identified with red dots in the top-right panel.

The CMD (left panel) shows the remarkably tight M4 main-sequence extending down to at least $V \sim 27$ on top of the foreground/background stars. A rich cluster white-dwarf cooling sequence is also seen stretching from $23 \leq V \leq 29.5$. As mentioned earlier, the line of sight through M4 ($d_{\text{M4}} = 1.7$ kpc) also intersects the spheroid of our Galaxy at a projected distance of 2.2 kpc above the Galactic nucleus (for a tangent point distance of 7.6 kpc). This population is more easily seen when the M4 main-sequence stars are removed by proper-motion selection (right panel). The field population clearly extends to $V \sim 30$

and shows some evidence for potential white dwarfs in the faint-blue region of the CMD. These can be clearly confused with the galaxies in the V , $V-I$ plane, thereby illustrating the importance of stellarity measurements.

The main sequence of the field population in the range $V = 24-30$ is too broad to be consistent with the color distribution expected from a population with no metallicity spread, at the distance of the spheroid. However, we can rule out a contribution of stars in these data from the Galactic bulge given that the line of sight passing through M4 lies well outside the infrared bulge as imaged by *COBE* (Arendt et al. 1998). The field also misses the highest surface-brightness isophotes in Binney, Gerhard & Spergel (1997) and clearly avoids the classical metal-rich bulge population (McWilliam & Rich 1994; Frogel, Tiede & Kuchinski 1999). Similarly, the redder stars in the field cannot be stars in the tri-axial bar near the Galactic center. The orientation of the bar is such that the near side of the semi-major axis (~ 2 kpc) lies in the first quadrant. The angle between the Sun-center line and the bar’s major axis in the plane of the disk is $\phi \sim 20^\circ$ (Gerhard 2002). The line of sight through M4 to the center of the Galaxy, $(l, b) = (350.97^\circ, 15.97^\circ)$ also falls in this quadrant. Given the thickness of the bar and axis ratio 1.0:0.6:0.4 (Binney, Gerhard & Spergel 1997), an azimuthal angle of 20° would place the near side of the bar major-axis only ~ 6.5 kpc from us (assuming an 8 kpc Galactocentric distance). However, with a latitude of $\sim 16^\circ$, the line of sight through M4 is already 1.9 kpc above the plane at a distance of 6.5 kpc and therefore well above the thickness of the bar. Other bar models, such as that in Cole & Weinberg (2002), would also not intersect our line of sight.

A better explanation for the thickness of the main sequence is that a small admixture of metal-rich thick disk stars along the line of sight make up the redder population. This is expected in these data given that the scale height of the thick disk is 1-1.5 kpc (Kuijken & Gilmore 1991; Bienaymé, Robin & Crézé 1987). These would be co-rotating, perhaps with a small lag, and therefore reside closer to the location of the galaxies. However, the proper-motion diagram does not show any obvious evidence of this population even when isolating only the reddest, brightest possible thick disk stars. The exact interpretation of the thickness of the observed main sequence is therefore still somewhat unclear and currently under investigation.

5. White Dwarfs

5.1. The Reduced Proper Motion Diagram

With galaxies clearly separated from stars in these data, finding spheroid/dark halo white dwarfs should be relatively easy considering they must be faint, blue and have a proper motion consistent with the spheroid clump. Since we also may have contamination from the thin and thick disk along our line of sight, the best way to isolate the inner-halo white dwarfs is to select them from the reduced proper motion diagram (RPMD). This two dimensional plot (H_V vs $V-I$, where $H_V = V + 5\log(\mu_{\text{total}}) + 5$, and μ_{total} is measured in "/yr) removes the different distances of individual populations by using the size of the proper motion as an effective distance indicator to offset the apparent magnitude. Therefore, similar populations, despite their distance, will occupy similar regions on this diagram based both on their stellar properties and kinematics. Figure 5 presents our stellar objects (stellarity > 0.7) for the large field clump (see Figure 4) on this plane together with the M4 stars (red dots).

The RPMD clearly shows that the majority of our spheroid main-sequence sample (small dark dots) is similar to M4 (red dots). This is expected considering the mean properties, such as the age and metallicity, are similar for both M4 and the spheroid. For a fixed magnitude, we see objects both above and below the M4 main-sequence stars on this plane. The objects above represent those with smaller proper motions (Pop I) and those below have greater proper motions (Pop II). The M4 white-dwarf cooling sequence is seen towards the blue end of the diagram and represents a locus for potential halo white dwarfs. Several candidate white dwarfs from the field population (larger dark dots) are clearly seen sprinkled through the range $14 \lesssim H_V \lesssim 25$, near $V-I \sim 1$. Most of these objects are found above the M4 white dwarfs, suggesting they have smaller proper motions (disk objects). Three objects are found below the M4 white dwarfs suggesting possible spheroid stars. Also shown are the locations of the thick-disk and putative dark halo-white dwarfs from the Mendez (2002) study (green squares) and those from the Nelson et al. (2002) study (blue triangles). The faintest Mendez object as well as the faintest two Nelson objects agree very well in location with the M4 white dwarfs on the RPMD (these are the claimed dark halo detections, see §6 for further discussion). The remaining Mendez and Nelson objects are found above the M4 stars, suggesting a possible thick disk origin. These points have all been corrected to match the reddening and extinction along this line of sight.

We also note that we do not select white dwarfs based on their location in the color-magnitude diagram for a reason. One would naively expect that the spheroid white dwarfs should be consistent with the location of the M4 white dwarf cooling sequence shifted down

to the tangent point (3.2 magnitudes fainter). However we need to consider that the spheroid white dwarfs will occupy some depth in distance around the tangent point so there are both closer and farther objects. Since the luminosity function (Hansen et al. 2002) of white dwarfs at the tangent point rises sharply at a point fainter than our limiting magnitude, we can expect to be systematically biased to seeing some fraction of the fainter white dwarfs within the region of the rising luminosity function slope if they reside closer to us than the tangent point. Since these fainter white dwarfs are redder than their brighter counterparts, the locus of these points will shift the +3.2-magnitude fiducial up to brighter magnitudes, on a parallel slope to the white dwarf cooling sequence. Therefore, we can not use a color cut on the CMD to select these objects. The approach used below does not suffer from these effects.

5.2. Simulations

In order to assign our candidate white dwarfs to particular Galactic components, we need to model the underlying white dwarf populations. We model four such components; the thin disk (a double exponential with radial scale length 3 kpc and vertical scale height 0.3 kpc), thick disk (a double exponential with radial scale length 3 kpc and vertical scale height 1 kpc), spheroid/stellar halo (a power law with $\rho \propto r^{-3.5}$, where r is the spherical Galactocentric radius) and a putative ‘dark halo’ (a power law with $\rho \propto r^{-2}$). The Solar-neighborhood (white dwarf only) normalizations for the various components are taken to be $3.4 \times 10^{-3} M_{\odot}/pc^3$ (Holberg, Oswalt & Sion 2002) for the thin disk, $10^{-4} M_{\odot}/pc^3$ for the thick disk (Oppenheimer et al. 2001; Reid, Sahu & Hawley 2001), $3 \times 10^{-5} M_{\odot}/pc^3$ for the spheroid (Gould, Flynn & Bahcall 1995) and $1.4 \times 10^{-3} M_{\odot}/pc^3$ for the dark halo (corresponding to a fraction 20% of the dark matter density, as indicated by the MACHO group’s results, Alcock et al. 2000).

The above density laws are projected onto the line of sight, taking into account the increasing volume at larger distance (for fixed solid angle). Using the same white dwarf models as in Hansen et al. (2002), we derive Monte-Carlo realizations of the field white dwarf populations distributed along our line of sight. The thin, thick and spheroid populations are drawn from a population with progenitor IMF $dN/dM \propto M^{-2.6}$. The dark halo population is drawn instead from a population with a Chabrier IMF (Chabrier 1999; IMF2 in the notation of that paper). The models of Hurley, Pols & Tout (2000) were used to provide main-sequence lifetimes. The thin-disk population was assumed to be forming stars at a continuous rate (over the past 10 Gyr) while all the others were assumed to be 12 Gyr old bursts. The Monte-Carlo calculations include the detection probability using the incompleteness corrections from Richer et al. (2002) and Hansen et al. (2002).

The final results indicate that, on average, we expect 7.9 thin-disk, 6.3 thick-disk and 2.2 spheroid white dwarfs. The dark halo will contribute 2.5 white dwarfs if 20% of the dark halo is made up of DA white dwarfs. The first three (i.e., the standard) populations are dominated by bright white dwarfs located near the tangent point (even for the disk populations, as the radial exponential largely compensates for the decrease due to the vertical exponential, at least for this line of sight). The dark-halo population, on the other hand, is dominated by objects at distances $\sim 2\text{-}3$ kpc, a consequence of the bias inherent in the Chabrier IMF towards higher progenitor masses and thus shorter main-sequence lifetimes (corresponding to longer white dwarf incarnations). This results in an anticipated systematic color difference between any dark-halo white dwarfs (relatively red) and those from standard populations (relatively blue). We stress this applies particularly to our data set and does not necessarily extend to wider-field surveys.

5.3. Results

In Figure 6, we display the location of the white dwarfs in the RPMD. We also overlay the positions of the simulated sample of white dwarfs (open circles) on this diagram (for a much larger area than that observed). The thin-disk (top-left) and thick-disk (top-right) stars are generally found brighter than the spheroid (bottom-left) stars, with a limit at $H_V \sim 25$ beyond which there are very few disk white dwarfs. A similar threshold was used by Flynn et al. (2001) to separate disk and halo white dwarfs. They found that most dark halo white dwarfs would lie at $24.3 \leq H_V \leq 26.3$ and peak at $H_V \sim 25.3$ (corrected to the extinction along this line of sight). The *relative* numbers of simulated thin-disk, thick-disk and spheroid objects plotted in Figure 6 have been scaled to match the expectations in our data. The $H_V \sim 14$ cutoff at the top of the diagram indicates the saturation limit of our data. The simulated dark-halo white dwarfs (open circles, bottom-right) are clearly distinct from these conventional populations and are found at redder colors (for an explanation see §5.2). Also included on this panel are those objects which did not satisfy the stellarity or proper motion cut (small crosses) to show that the data do extend fainter than $H_V = 25$ and well into the dark halo regime.

Although it is difficult to separate thin-/thick-disk white dwarfs, we can conclude that nine of our objects are consistent with disk white dwarfs ($H_V \leq 23$, $V-I \leq 1.5$). Three objects in our data ($H_V = 23.15$, $V-I = 0.48$, $H_V = 23.78$, $V-I = 0.93$, and $H_V = 24.09$, $V-I = 0.93$) which are fainter than this cut are found within the tail of the thick disk simulated sample. These objects are however in excellent agreement with the simulated spheroid white dwarfs (bottom-left). These are also the three objects which fall below the M4

white dwarfs in Figure 5. Although the predicted number of stars allows for incompleteness in the data set, we must still correct these observed numbers of stars for the incompleteness caused by mismatches in the SExtractor vs ALLSTAR classifications. In §3.1 we estimated 25% of the ALLSTAR sources were missed for these magnitude bins. Our final corrected numbers of detected objects are therefore 12 disk white dwarfs (14 expected) and 4 spheroidal white dwarfs (2 expected) and therefore in good agreement with the predictions considering that the observed spheroidal number is an upper limit (i.e., two of the objects are consistent with the tail of the thick disk distribution).

A key result from Figure 6 is that the simulated dark halo region is basically not populated with data points. Only one object which we classified as thick disk, $H_V = 22.25$, $V-I = 1.38$, marginally agrees with the edge of the simulated sample (small open circles). Less than 4% of our simulated dark-halo sample is found with a reduced proper motion less than this object, suggesting <0.1 expected real objects. Also, the color of this star falls close to the blue edge of the simulated sample and is only marginally consistent with the expected location of dark-halo white dwarfs. A possible explanation for the other extremely red object, as well as possibly this object, is that these may be binary thin-/thick-disk white dwarfs with red main-sequence companions. We can also rule out the spheroidal candidate objects as potential dark-halo white dwarfs given that they have much bluer colors. We’ve added photometric and astrometric error bars to all candidates in the bottom-right panel of Figure 6. The errors are $1-\sigma$ values from the results of artificial star tests. For example, the magnitude and color errors are the input vs output photometric values and the positional errors are the input vs output coordinates in the tests. The H_V error combines the contribution from the magnitude and proper-motion terms. We have left these error bars off from other panels to prevent cluttering in the diagrams. We also note that just relaxing the stellarity cut to 0.5 would not allow any of the spurious sources (small crosses) to qualify as candidate dark halo white dwarfs given their inconsistent proper motions. Finally, we indicate the limit at $H_V \sim 27$ above which we would have expected dark-halo white dwarfs given our simulations and detection efficiency. Table 2 presents our final white dwarf candidate list, both for the disk and spheroidal.

6. Discussion

Contrary to our result, recent claims by Oppenheimer et al. (2001), Koopmans & Blandford (2001), Nelson et al. (2002) and Mendez (2002) suggest that a halo white-dwarf population exists and that the number of white dwarfs is in excess of that expected from the stellar spheroidal alone. Others (Reid, Sahu & Hawley 2001; Hansen 2001; Richer 2001) have

argued that this small population is a component of the thick disk. Gibson & Mould (1997) used simple chemical evolutionary arguments to show that it is difficult to reconcile the observed spheroid main-sequence chemical abundance with that expected from an IMF which would give the speculated halo white-dwarf density. We briefly summarize these independent studies and place them in the context of the present observations.

Oppenheimer et al. (2001) sampled 4165 sq. deg. towards the Southern Galactic Cap and found 38 cool white dwarfs, the majority of which they assign to a dark-halo population. The data from this study were made available and consequently several authors have re-analyzed the result. Koopmans & Blandford (2001) used a dynamical model and performed a maximum-likelihood analysis on the Oppenheimer sample of white dwarfs and found two kinematically distinct populations at a greater than 99% confidence limit (a thick disk and a flattened halo). However, Reid, Sahu & Hawley (2001) compared the kinematics of the Oppenheimer sample to the local M-dwarf sample and suggested that the majority of this population resides in the thick disk. Richer (2001) and Hansen (2001) examined the temperature and age distribution of the Oppenheimer white dwarf sample and found that the star-formation history for most of these stars is more representative of the disk rather than the halo.

The Nelson et al. (2002) study looked for high-proper-motion objects in the Groth-Westphal strip. They measured proper motions over a 7-year baseline using WFPC2 observations of a 74.8 arcmin² region. Of the 24 high-proper-motion objects detected, five are believed to be strong white dwarf candidates (two of these are dark halo, three are disk) and a further two are classified as marginal candidates. The two halo objects are the faintest two blue triangles in Figure 5 and the three disk objects are the brightest three blue triangles in Figure 5. By creating a model of the stellar components of our Galaxy, Nelson et al. (2002) demonstrate that the observations are clearly in excess of the expected number of white dwarfs from the Galactic stellar components. Although systematic errors due to uncertainties in the model parameters are large, the observations suggest a 7% white-dwarf dark halo.

Most recently, Mendez (2002) has presented new evidence for a bi-modal kinematic population of old white dwarfs and suggests that most of the required dark matter in the Solar vicinity can be accounted for by these populations. This analysis is based on a proper-motion membership study of the Galactic globular cluster NGC 6397 (King et al. 1998). Mendez (2002) used both the reduced proper motion and the colors of field objects to assign six white-dwarf candidates to the thick disk and one to the dark halo (the faintest green square shown in Figure 5). The Mendez (2002) study gives no information on the morphology of the sources and possible extragalactic contamination.

There is clearly no convincing answer yet as to whether white dwarfs make up an important component of the dark matter in our Galaxy. The controversy spurred from these studies can only be resolved by obtaining deeper, larger images of halo fields which could contain many white dwarfs. The current data set represents an important constraint in the context of searching for these objects as it is sensitive to white dwarfs from all three (disk, spheroid and dark-halo) components and it is only the dark-halo ones that are not found. Furthermore, our images represent the deepest-ever probe into the inner halo of our Galaxy and we do see the stellar halo main-sequence progenitors of the white dwarfs. By using only directly observable quantities, such as the proper motions, magnitudes and colors we have demonstrated that these data do not support a white-dwarf component to the dark halo.

7. Conclusions

A 6-year baseline of imaging of the globular star cluster M4 has allowed us to separate out the cluster stars from the background spheroid population. Over this time, distant extragalactic sources have not moved and are identified using image morphology criteria. We establish a zero-motion frame of reference using these galaxies and search for halo white dwarfs based on their morphology and kinematics. We find that distinguishing faint galaxies from field stars is impossible when based solely on proper motions, and that an index of stellarity is crucial in separating the two classes. Based on the reduced proper motion diagram, we identify nine thin/thick disk and three spheroid white dwarfs in these data. These numbers are consistent with the expected contribution of the conventional populations along the line of sight. Additionally, 2.5 dark halo white dwarfs are expected in these data based on a 20% white dwarf dark halo and are not found. Therefore, we do not need to invoke a dark halo population of white dwarfs to explain the present data.

The extragalactic reference frame also allows us to perform two other important measurements. First, this fixed frame gives us an independent measurement of the fundamental Galactic constant, $\Omega_{\circ} = \Theta_{\circ}/R_{\circ} = 25.3 \pm 2.6$ km/s/kpc. This provides a velocity of the Local Standard of Rest $v_{\text{LSR}} = \Theta_{\circ} = 202 \pm 25$ km/s at $R_{\circ} = 8.0 \pm 0.5$ kpc, in agreement with independent studies. Secondly, the galaxies give us a direct measurement of M4’s absolute proper motion, $\mu_{\alpha}\hat{\alpha} = -12.26 \pm 0.54$ mas/yr, $\mu_{\delta}\hat{\delta} = -18.95 \pm 0.54$ mas/yr, also in good agreement with the latest studies.

The author wishes to thank C.A. Nelson et al. for making available their simulated white dwarfs and D.I. Dinescu for useful information about coordinate conversions. We also acknowledge I. King & S. Courteau for useful discussions regarding the circular speed curve

and P. Guhathakurta for pointing out an important oversight in a preliminary version of this paper. JSK received financial support during this work through an NSERC PGS-B graduate student research grant. HBR is supported in part by the Natural Sciences and Engineering Research Council of Canada. HBR also extends his appreciation to the Killam Foundation and the Canada Council for the award of a Canada Council Killam Fellowship. RMR and IS acknowledges support from proposal GO-8679 and BMH from a Hubble Fellowship HF-01120.01 both of which were provided by NASA through a grant from the Space Telescope Science Institute which is operated by AURA under NASA contract NAS5-26555. BKG acknowledges the support of the Australian Research Council through its Large Research Grant Program A00105171.

REFERENCES

- Alcock, C., Allsman, R. A., Alves, D. R., Axelrod, T. S., Becker, A. C., Bennett, D. P., Cook, K. H., Dalal, N., Drake, A. J., Freeman, K. C., Geha, M., Griest, K., Lehner, M. J., Marshall, S. L., Minniti, D., Nelson, C. A., Peterson, B. A., Popowski, P., Pratt, M. R., Quinn, P. J., Stubbs, C. W., Sutherland, W., Tomaney, A. B., Vandehei, T., & Welch, D. 2000, *ApJ*, 542, 281
- Arendt, R. G., Odegard, N., Weiland, J. L., Sodroski, T. J., Hauser, M. G., Dwek, E., Kelsall, T., Moseley, S. H., Silverberg, R. F., Leisawitz, D., Mitchell, K., Reach, W. T., & Wright, E. L. 1998, *ApJ*, 508, 74
- Backer, D., & Stramek R. A. 1999, *ApJ*, 524, 805
- Bedin, L. R., Piotto, G., King, I. R., & Anderson, J. 2003, submitted
- Bertin, E., & Arnouts, S. 1996, *A&AS*, 117, 393
- Bienaymé, O., Robin, A. C., & Crézé, M. 1987, *A&A*, 180, 94
- Binney, J., & Merrifield, M. 1998, *Galactic Astronomy* (Princeton: University Press)
- Binney, J., Gerhard, O., & Spergel, D. 1997, *MNRAS*, 288, 365
- Binney, J., & Tremaine, S. 1987, *Galactic Dynamics* (Princeton: University Press)
- Biretta, L. et al. 2002, *WFPC2 Instrument Handbook, Version 7.0* (Baltimore: STScI)
- Chabrier, G. 1999, *ApJ*, 513, L103
- Cole, A. A., & Weinberg, M. D. 2002, *ApJ*, 574, L43

- Cudworth, K. M., & Rees, R. 1990, *AJ*, 99, 1491
- Dehnen, W., & Binney, J. J. 1998, *MNRAS*, 298, 387
- Dinescu, D. I., van Altena, W. F., Girard, T. M., & Lopez, C. E. 1999, *AJ*, 117, 277
- Dinescu, D. I., van Altena, W. F., Girard, T. M., & Lopez, C. E. 1997, 191st AAS Meeting, 98.03, *Bulletin of the American Astronomical Society*, 29, 1367
- Djorgovski, S. 1993, in *ASP Conf. Proc. 50, Structure and Dynamics of Globular Clusters*, ed. S. G. Djorgovski, & G. Meylan (San Francisco: ASP), 373
- Feast, M., & Whitelock, P. 1997, *MNRAS*, 291, 683
- Flynn, C., Sommer-Larsen, J., Fuchs, B., Graff, D. S., Salim, S. 2001, *MNRAS*, 322, 553
- Frogel, J. A., Tiede, G. P., & Kuchinski, L. E. 1999, *AJ*, 117, 2296
- Gerhard, O. 2002, *ASP Conf. Proc. 273, The Dynamics, Structure & History of Galaxies: A Workshop in Honour of Professor Ken Freeman*, ed. G. S. Da Costa & H. Jerjen (San Francisco: ASP), 73
- Gibson, B. K., & Mould, J. R. 1997, *ApJ*, 482, 98
- Hansen, B. M. S., Brewer, J., Fahlman, G. G., Gibson, B. K., Ibata, R., Limongi, M., Rich, R. M., Richer, H. B., Shara, M. M., & Stetson, P. B. 2002a, *ApJ*, 574, L155
- Hansen, B. M. 2001, *ApJ*, 558, L39
- Hansen, B. M. 1999, *ApJ*, 520, 680
- Holberg, J. B., Oswalt, R. D., & Sion, E. M. 2002, *ApJ*, 571, 512
- Hurley, J. R., Pols, O. R. & Tout, C. A. 2000, *MNRAS*, 315, 543
- Ibata, R. A., Richer, H. B., Fahlman, G. G., Bolte, M., Bond, H. E., Hesser, J. E., Pryor, C., & Stetson, P. B. 1999, *ApJS*, 120, 265
- Kerr, F. J., & Lynden-Bell, D. 1986, *MNRAS*, 221, 1023
- King, I. R., Anderson, J., Cool, A. M., & Piotto, G. 1998, *ApJ*, 492, L37
- Koopmans, L. V. E., & Blandford, R. D. 2001, submitted to *MNRAS* (astro-ph/0107358)
- Kuijken, K., & Tremaine, S. 1994, *ApJ*, 421, 178

- Kuijken, K., & Gilmore, G. 1991, *ApJ*, 367, L9
- McWilliam, A., & Rich, R. M. 1994, *ApJS*, 91, 749
- Mendez, R. A. 2002, *A&A*, 395, 779
- Merrifield, M. R. 1992, *AJ*, 103, 1552
- Nelson, C. A., Cook, K. H., Axelrod, T. S., Mould, J. R., & Alcock, C. 2002, *ApJ*, 573, 644
- Oppenheimer, B. R., Hambly, N. C., Digby, A. P., Hodgkin, S. T., & Saumon, D. 2001, *Science*, 292, 698
- Peterson, R. C., Rees, R. F., & Cudworth, K. M. 1995, *ApJ*, 443, 124
- Reid, I. N., Sahu, K. C., & Hawley, S. L. 2001, *ApJ*, 559, 942
- Reid, M. J., Readhead, A. C. S., Vermeulen, R. C., & Treuhaft, R. N. 1999, *ApJ*, 524, 816
- Richer et al. 2003, in preparation
- Richer, H. B., Brewer, J., Fahlman, G. G., Gibson, B. K., Hansen, B. M., Ibata, R., Kalirai, J. S., Limongi, M., Rich, R. M., Saviane, I., Shara, M. M., & Stetson, P. B. 2002, *ApJ*, 574, L151
- Richer H.B. 2001, astro-ph/0107079
- Richer, H. B., Fahlman, G. G., Ibata, R. A., Pryor, C., Bell, R. A., Bolte, M., Bond, H. E., Harris, W. E., Hesser, J. E., Holland, S., Ivanans, N., Mandushev, G., Stetson, P. B., & Wood, M. A. 1997, *ApJ*, 484, 741
- Richer, H. B., Fahlman, G. G., Ibata, R. A., Stetson, P. B., Bell, R. A., Bolte, M., Bond, H. E., Harris, W. E., Hesser, J. E., Mandushev, G., Pryor, C., & Vandenberg, D. A. 1995, *ApJ*, 451, L17
- Saviane, I. et al. 2003, in preparation
- Stetson, P. B. 1987, *PASP*, 99, 191
- Stetson, P. B. 1994, *PASP*, 106, 250
- Terndrup, D. M., Popowski, P., Gould, A., Rich, R. M., Sadler, E. M. 1998, *AJ*, 115, 1476
- Wilkinson, M. I., & Evans, N. W. 1995, *MNRAS*, 310, 645

Williams, R. E., Blacker, B., Dickinson, M., Dixon, W. Van Dyke, Ferguson, H. C., Fruchter, A. S., Giavalisco, M., Gilliland, R. L., Heyer, I., Katsanis, R., Levay, Z., Lucas, Ray A., McElroy, D. B., Petro, L., Postman, M., Adorf, Hans-Martin., & Hook, R. 1996, *AJ*, 112, 1335

Fig. 1.— Figure 1: The proper-motion diagram for all stars ($\mu_l \hat{\mathbf{l}}, \mu_b \hat{\mathbf{b}}$) is shown with galaxies represented as red dots (see §3). The vector proper motions are expressed using the convention where $\hat{\mathbf{l}}$ and $\hat{\mathbf{b}}$ are unit vectors in the corresponding directions. The galaxies used to determine the zero-motion reference frame are displayed as larger dots (see §3.2). The tighter clump of M4 stars is clearly distinct from the more diffuse spheroid clump.

Fig. 2.— Figure 2: *Top* - A plot of stellarity vs magnitude shows that we have clearly separated stars from galaxies down to $V \sim 29$. *Bottom* - The stellarity of all objects is plotted against the total proper-motion displacement ($\mu_{\text{total}} = \sqrt{(\mu_l \hat{\mathbf{l}})^2 + (\mu_b \hat{\mathbf{b}})^2}$) to illustrate the different populations along the M4 line of sight (see §3.1).

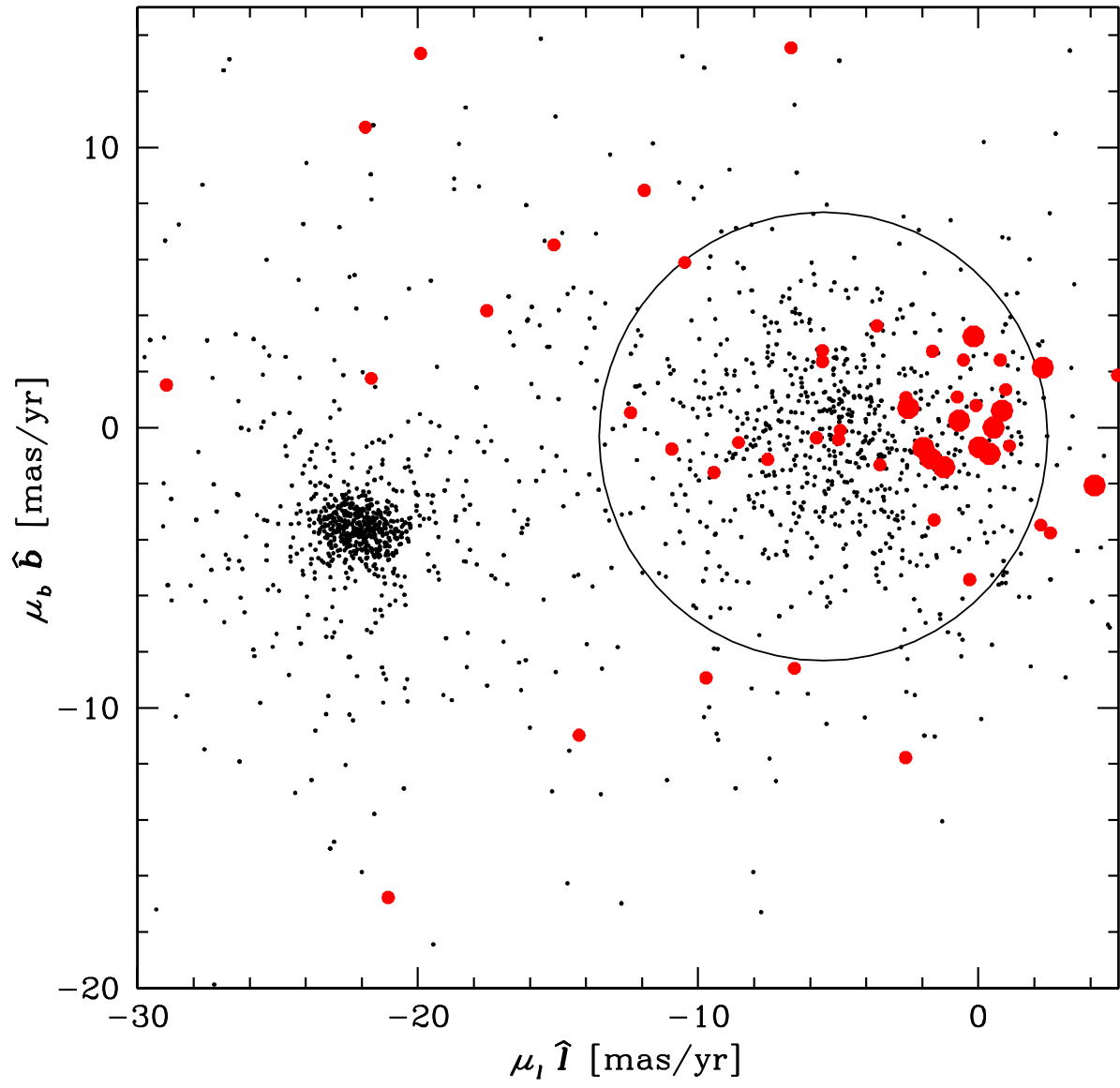
Fig. 3.— Figure 3: The total proper motion displacement is plotted as a function of V magnitude for both stars (*top*) and galaxies (*bottom*) as determined by SExtractor. The stars are found along two sequences, representing the cluster ($\mu_{\text{total}} \sim 22.5$ mas/yr) and the spheroid ($\mu_{\text{total}} \sim 5$ mas/yr) populations. The galaxies are confined to zero motion for $V \lesssim 27$, beyond which their astrometry degrades (see §3.2). These brightest galaxies are used to define the zero-motion frame of reference.

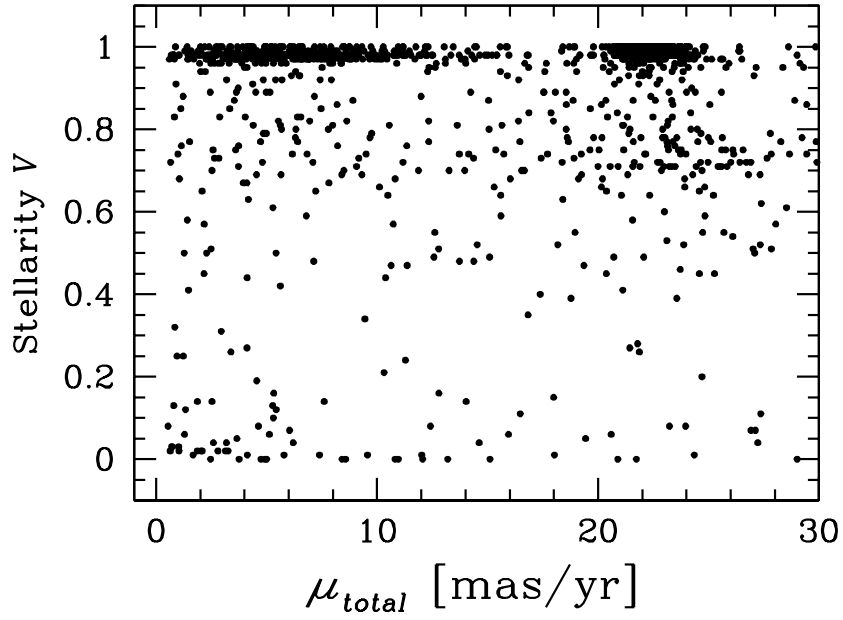
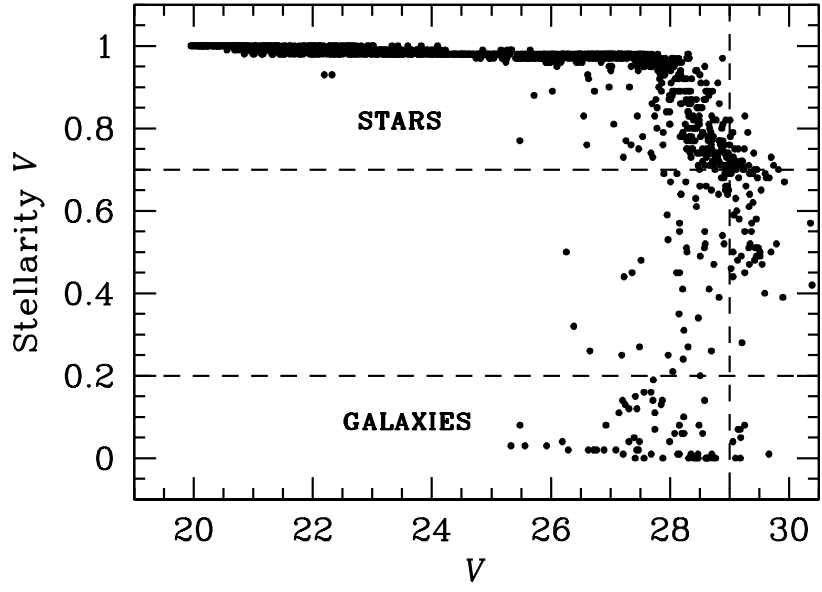
Fig. 4.— Figure 4: *Top* - The proper-motion diagram for all stars ($\mu_l \hat{\mathbf{l}}, \mu_b \hat{\mathbf{b}}$) is shown with galaxies represented as red dots (see §3). The tighter clump represents M4 members and the more diffuse clump predominantly represents the background spheroid stars. *Bottom* - The CMD for all objects in the image is shown (left panel) and for only those objects which fall within the spheroid field clump (right panel). The galaxies are shown in red.

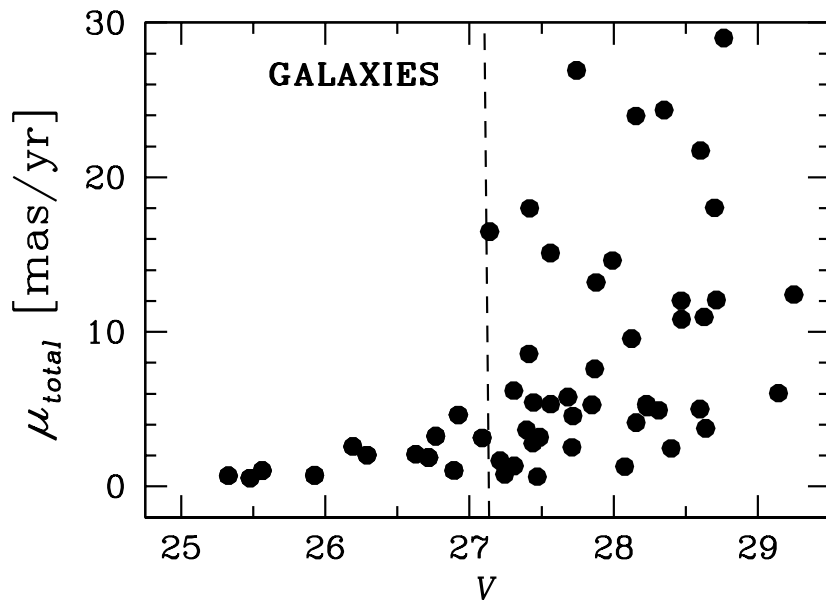
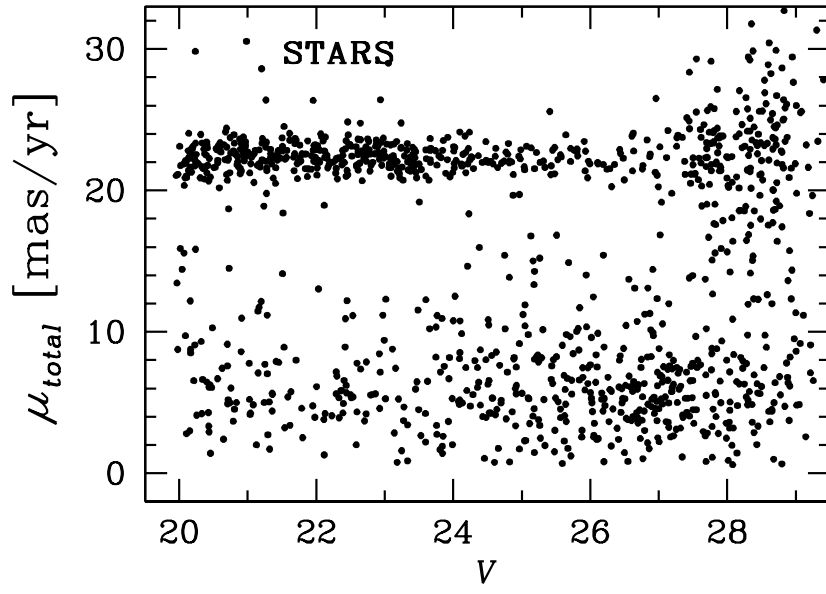
Fig. 5.— Figure 5: The reduced proper motion diagram ($H_V = V + 5 \log(\mu_{\text{total}}'') + 5$) is shown for all field stars with stellarity > 0.7 and M4 members (red dots). Inner halo white dwarf candidates are displayed with larger circles. White dwarfs from the Mendez 2002 study (green squares) and the Nelson et al. 2002 study (blue triangles) are also displayed after correcting for reddening and extinction differences.

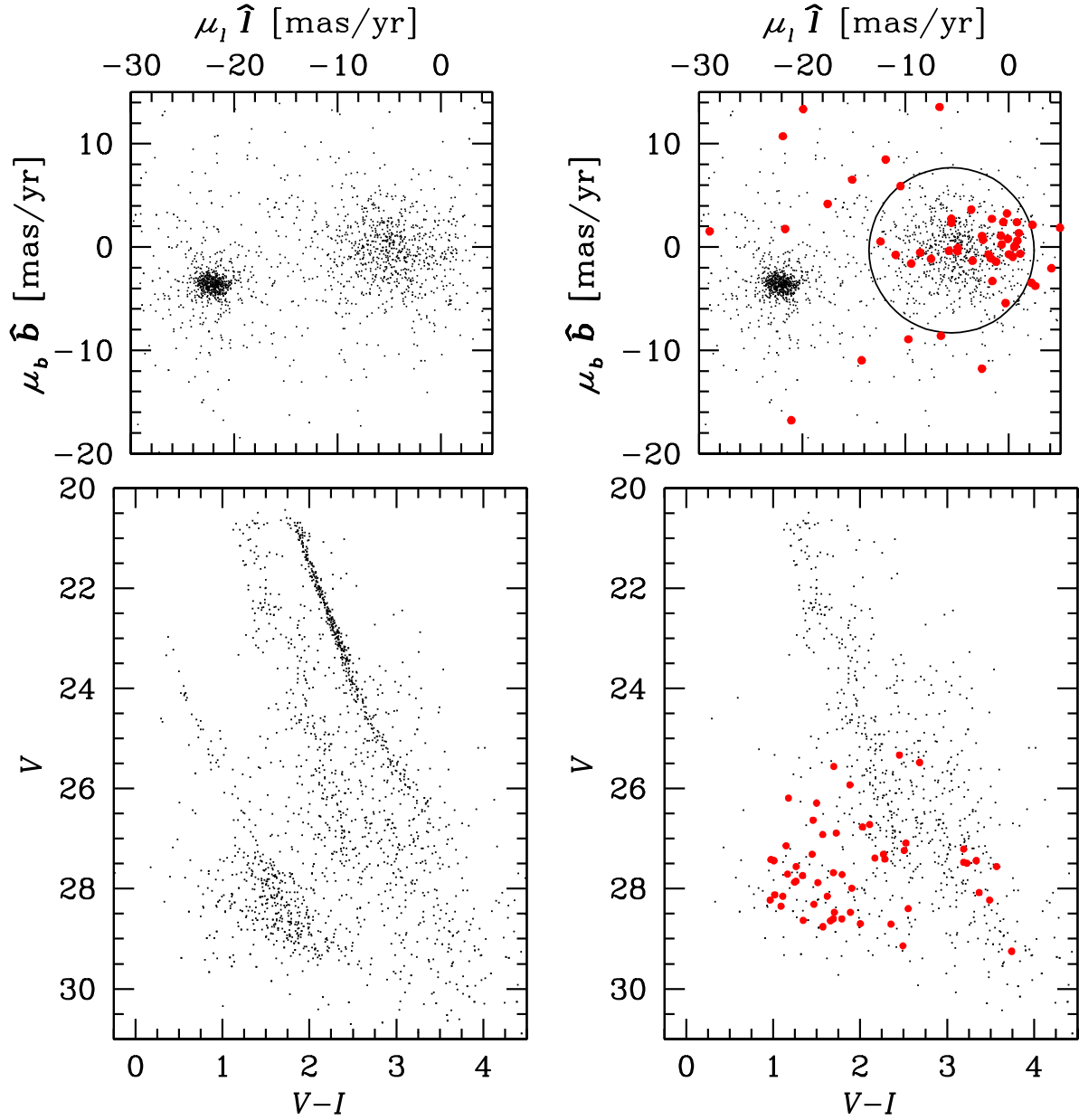
Fig. 6.— Figure 6: A simulated sample of stars belonging to the thin disk (top-left), thick disk (top-right), spheroid (bottom-left) and dark halo (bottom-right) are shown on the RPMD as small open circles in all panels. Candidate white dwarfs from the present data are shown as large filled circles. After correcting for mismatches in the SExtractor vs ALLSTAR photometry, we find 12 (9 originally) thin/thick disk white dwarfs and 4 (3 originally) spheroid white dwarfs. Although 2.5 objects are expected from a 20% dark halo dominated by white dwarfs, we find none in these data (see §5.3). $1-\sigma$ astrometric and photometric error bars for all candidates are only shown in the bottom-right panel to prevent cluttering in other panels. Small crosses depict those objects which did not satisfy the stellarity or

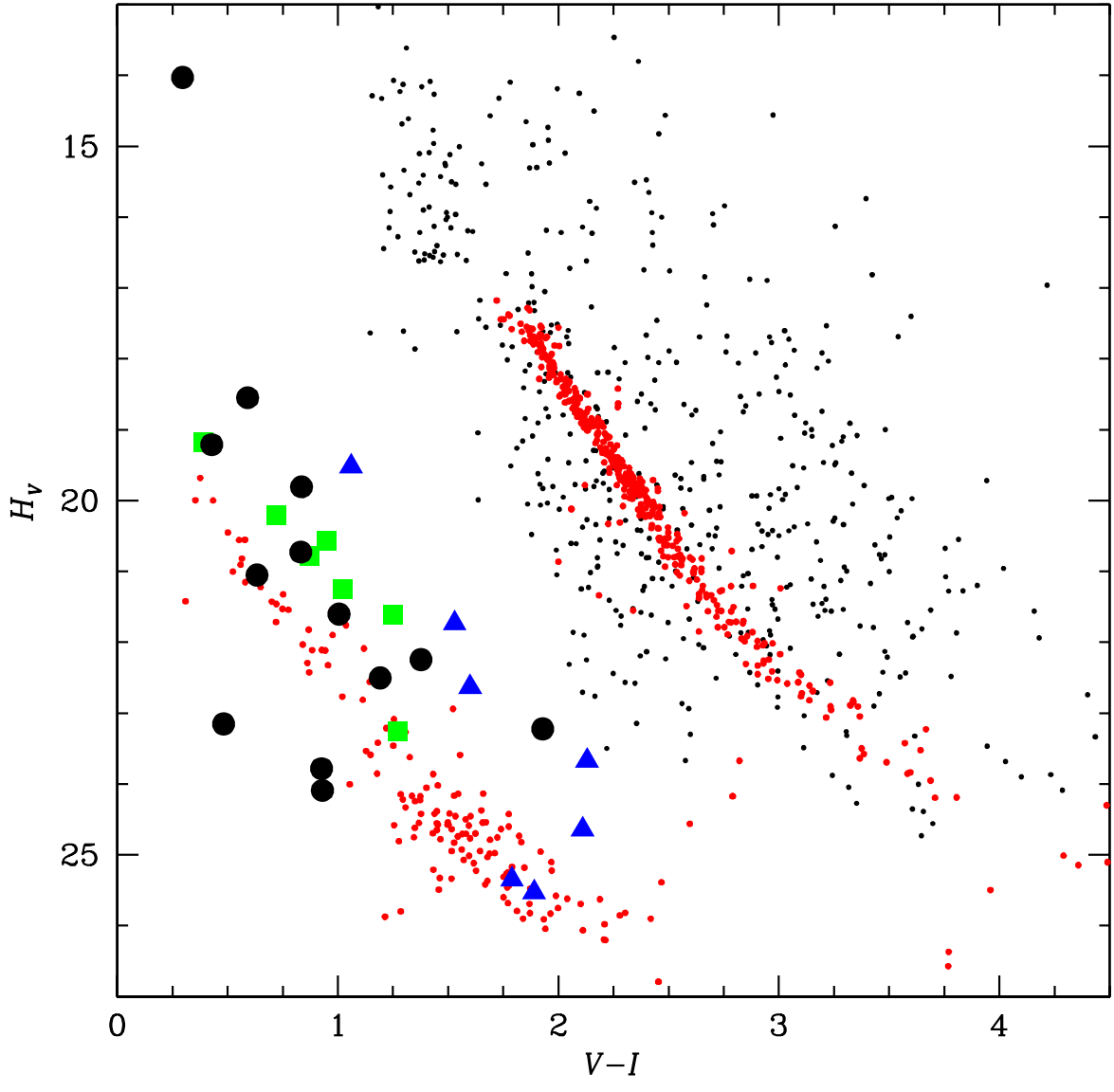
proper motion cut and show that the data set is sensitive to $H_V \lesssim 27$ (and therefore to dark halo white dwarfs).











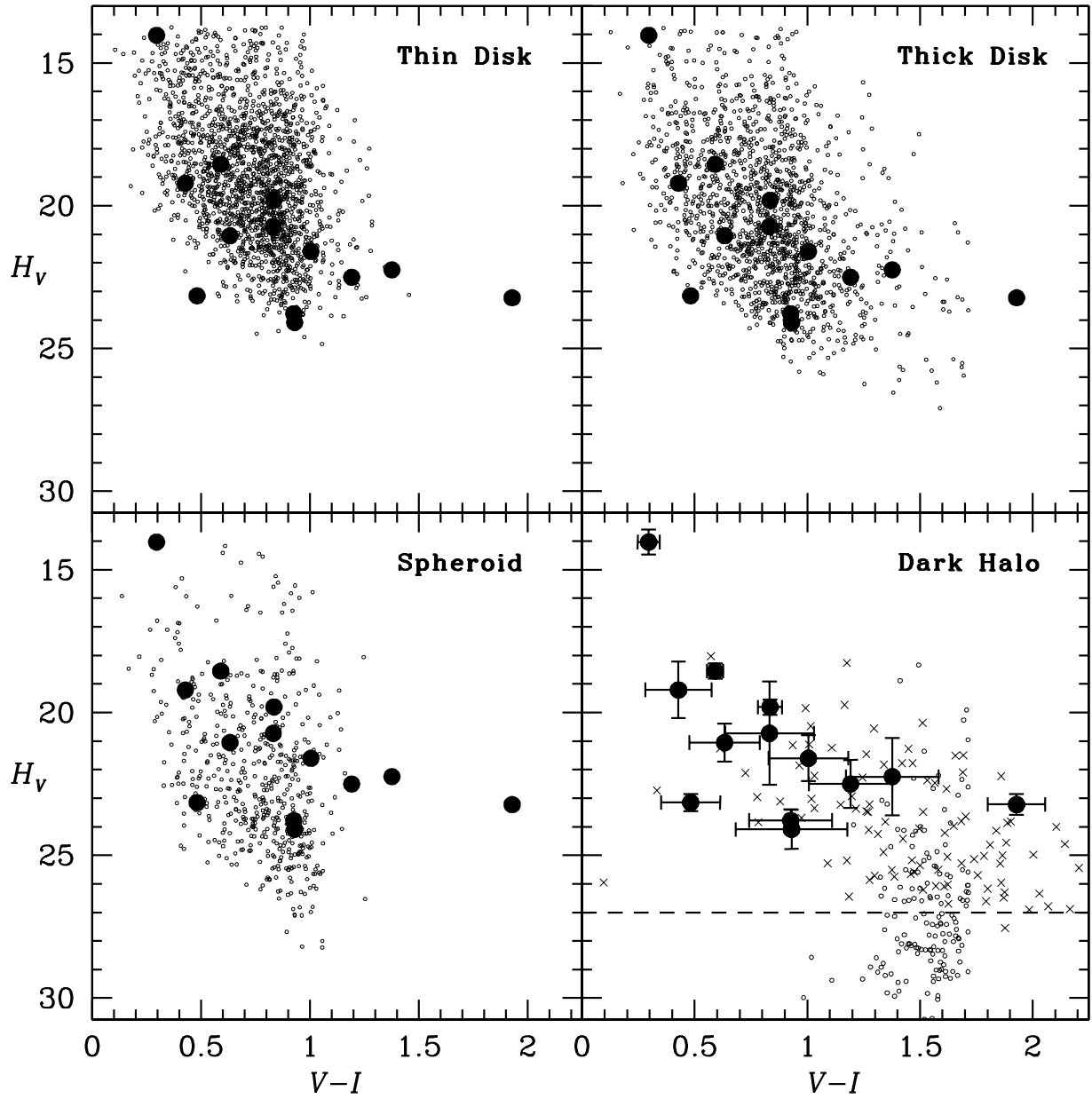


Table 1. Cluster, Field Parameters and Observational Data

Field Location:		
α_{J2000}	RA	= $16^{\text{h}}23^{\text{m}}54.6^{\text{s}}$
δ_{J2000}	declination	= $-26^{\circ}32'24.3''$
l_{J2000}	Galactic longitude	= 351.01°
b_{J2000}	Galactic latitude	= 15.91°
Cluster Distance & Reddening ¹ :		
$(m-M)_V$	apparent distance modulus	= 12.51
$E(B-V)$	reddening	= 0.35
A_V	visual extinction	= 1.33
$(m-M)_{\odot}$	true distance modulus	= 11.18
d	distance from Sun	= 1.72 kpc
Background Field (Spheroid) Distance & Reddening:		
$(m-M)_V$	apparent distance modulus	= 15.71
$E(B-V)$	reddening (all in front of M4)	= 0.35
A_V	visual extinction	= 1.33
$(m-M)_{\odot}$	true distance modulus	= 14.39
d	tangent point distance	= 7.6 kpc
z	projected distance from Nucleus	= 2.2 kpc
Metallicity (Cluster ² & Spheroid:		
$[Fe/H]$	heavy metal abundance	= -1.3
Data (GO 5461 ³ - cycle 4 & GO 8679 - cycle 9):		
No. of Images – F555W - 1995	15×2600 seconds	
No. of Images – F606W - 2001	98×1300 seconds	
No. of Images – F814W - 1995	9×800 seconds	
No. of Images – F814W - 2001	148×1300 seconds	
Limiting Magnitude (Based on SExtractor Classifications):		
V	29	
I	27.5	

References. — 1. Richer et al (1997), 2. Djorgovski (1993), 3. Ibata et al (1999)

Table 2. Disk and Spheroid White Dwarfs

Candidate	Designation	α_{J2000}	δ_{J2000}	V	$V-I$	μ (mas/yr) ¹	$\mu_l \hat{\mathbf{l}}$ (mas/yr)	$\mu_b \hat{\mathbf{b}}$ (mas/yr)
WD 1	disk	16:23:52.76	-26:33:13.07	24.60	0.30	0.77	0.77	-0.05
WD 2	disk	16:23:54.49	-26:31:19.38	27.17	0.43	2.56	2.33	1.06
WD 3	disk	16:23:55.54	-26:32:36.64	24.18	0.59	7.47	-7.27	-1.71
WD 4	disk	16:23:55.87	-26:33:03.28	27.43	0.63	5.31	-5.22	0.96
WD 5	disk	16:23:58.75	-26:32:40.13	25.22	0.84	8.28	-8.26	0.51
WD 6	disk	16:24:02.33	-26:32:25.55	27.98	0.83	3.54	0.88	3.43
WD 7	disk	16:24:02.81	-26:32:42.61	27.82	1.01	5.70	-5.37	-1.91
WD 8	disk	16:24:03.10	-26:32:45.10	27.99	1.19	7.99	-7.41	-3.01
WD 9	spheroid	16:23:55.28	-26:32:47.47	27.02	0.48	16.85	-15.48	6.66
WD 10	spheroid	16:23:55.87	-26:32:37.77	28.34	0.93	14.15	-13.69	3.57
WD 11	spheroid	16:23:58.12	-26:32:10.13	27.82	0.93	15.58	-15.31	2.89
WD 12	disk?	16:23:53.25	-26:33:10.66	28.25	1.38	6.30	-4.73	-4.17
WD 13	disk?	16:23:59.35	-26:31:28.52	27.49	1.93	13.99	-13.89	-1.67

$$^1\mu_{\text{total}} = \sqrt{(\mu_l \hat{\mathbf{l}})^2 + (\mu_b \hat{\mathbf{b}})^2}$$